IOPscience iopscience.iop.org

Home Search Collections Journals About Contact us My IOPscience

Characterization of a micromachined parylene-based thermal C-shape actuator

This article has been downloaded from IOPscience. Please scroll down to see the full text article.

2011 J. Micromech. Microeng. 21 095028

(http://iopscience.iop.org/0960-1317/21/9/095028)

View the table of contents for this issue, or go to the journal homepage for more

Download details:
IP Address: 130.64.2.235
The article was downloaded on 20/08/2011 at 02:16

Please note that terms and conditions apply.

IOP PUBLISHING JOURNAL OF MICROMECHANICS AND MICROENGINEERING

J. Micromech. Microeng. **21** (2011) 095028 (10pp) doi:10.1088/0960-1317/21/9/095028

Characterization of a micromachined parylene-based thermal C-shape actuator

Minchul Shin[1], Aaron P Gerratt[2], Cinzia Metallo[3], Alex Brindle[1], Brian P Kierstead[1] and Robert D White[1]

[1] Department of Mechanical Engineering, Tufts University, Medford, MA, USA
[2] Department of Mechanical Engineering, University of Maryland, College Park, MD, USA
[3] Department of Neuroscience, Tufts University, School of Medicine, Boston, MA, USA

E-mail: r.white@tufts.edu

Received 18 January 2011, in final form 21 July 2011
Published 19 August 2011
Online at stacks.iop.org/JMM/21/095028

Abstract
This paper describes the design, fabrication and characterization of parylene-based C-shape actuators. The actuators flatten out in response to temperature changes created by ohmic heating of built-in thin film resistors. The devices are fabricated by micromachining processes using parylene C and four metal layers. Mathematical modeling of operation temperature, displacement and load capacity was carried out and verified experimentally. The device operates on less than 0.33 V input voltage and 90 mA input current. During operation, the temperature of the actuator is less than 32 °C. This actuator has an 11 μN load capacity, 5 mm of tip displacement and a bandwidth of 1.4 Hz.

(Some figures in this article are in colour only in the electronic version)

1. Introduction

Micro-electro-mechanical systems (MEMS) continue to grow more complicated and multifunctional. These systems often include both sensing and actuating capabilities that are required for various applications. Actuation subsystems are of primary importance for all types of microscale manipulation and locomotion. Micro-motion systems such as microrobots, microconveyers, or microgrippers can benefit from microactuators with both large displacements and high forces. For certain applications, such as cell manipulation, actuator temperature is also of primary importance. In recent years, many kinds of microactuators have been developed using MEMS technologies. MEMS actuators can be categorized by the actuation method, including thermal [1–14], pneumatic [15–18], piezoelectric [19, 20], electrostatic [21, 22], electromagnetic [23, 24] and shape memory alloy effect [25, 26]. Many additional examples can be found in the literature.

In this paper we focus on a thermal multimaterial system, which consists of two or more material layers with different thermal expansion coefficients. As the device temperature changes, differential thermal expansion causes the device to deflect. Micro-motion systems using the thermal bimaterial principle have a simple fabrication process, high driving force and large displacement. However, these actuators require considerable power consumption, a long cooling time, which may result in a small bandwidth, and may require a large area on the chip to achieve high enough forces for certain applications. To completely characterize such systems, a variety of metrics need to be considered, including displacement, force, actuation bandwidth and temperature. Both measurements and models of these characteristics are needed to fully understand their connection and to develop tools that can be used for designing and optimizing thermal actuators. A major goal of this paper is to present force, deflection, temperature, and bandwidth measurements alongside mathematical models in order to validate the models.

Table 1 gives a list of thermal actuators as described by various authors. Some authors focus on modeling, whereas others focus on experimental characterization or specific applications. No author has both described comprehensive mechanical, thermal and dynamic models as well as presented a set of measurements to directly compare to those models. In addition, the majority of authors measure deflection but do not measure temperature or force. To the best of our knowledge, only Kim *et al* give complete force characterization data [7]. Comtois and Bright state the value of tip force but provide little

 © 2011 IOP Publishing Ltd Printed in the UK & the USA

Table 1. Examples of some MEMS thermal actuation systems.

Author	Principle	Actuator length	Maximum force	Bandwidth	Maximum displacement
Riethmuller and Benecke 1988 [9]	Silicon bimorph cantilever	500 μm	Not specified	Not specified	100 μm
Doring *et al* 1992 [13]	Aluminum and silicon bimorph	1–2 mm	Not specified	1 kHz	150 μm
Ataka *et al* 1993 [1]	Polyimide array	500 μm	Not specified	10 Hz	150 μm
Lin *et al* 1995 [8]	Polyimide gripper	100 μm	Not specified	10 Hz	70 μm
Suh *et al* 1997 [10]	Polyimide array	430 μm	Not specified	Not specified	125 μm
Comtois and Bright 1997 [4]	Polysilicon actuators and arrays	150–240 μm	15.5 μN	1 kHz	16 μm
Kladitis and Bright 2000 [12]	Polysilicon hinged array	270 μm	Not specified	3 Hz	3.75 μm
Ebefors *et al* 2000 [5]	Silicon array with polyimide joint	500 μm	Not specified	3 Hz	170 μm
Enikov and Lazarov 2003 [6]	Nickel actuator	600 μm	Not specified	1 kHz	13 μm
Zhou *et al* 2004 [2, 14]	Parylene gripper	2 mm	Not specified	3 Hz	Not specified
Chronis and Lee 2005 [3]	SU-8 thermal micro-gripper	650 μm	Not specified	4.8 Hz	6 μm
Wu and Hsu 2006 [11]	Bi level polyimide actuator	400 μm	Not specified	Not specified	20 μm
Kim *et al* 2008 [7]	Silicon gripper with v-beam actuator and force feedback	Not specified	58 μN	5 Hz	67 μm
Current work	Parylene-based thermal actuator	1.25 mm	11 μN	1.4 Hz	260 μm

description of measurement methods, nor do they provide data for force plotted against temperature or power [4]. A number of authors working on microrobotics or microconveyers measure the maximum load that the locomotion system can carry without stalling, but do not directly measure actuator tip force (e.g. [5, 10, 12]). Doring *et al*, Ataka *et al*, Ebefors *et al* include temperature measurements [1, 5, 13]. Riethmuller and Benecke demonstrated one of the earliest silicon thermal actuators in 1988, and described a mechanical model and a limited thermal model, but did not have measurements of force or temperature to compare with their models [9]. Chu *et al* present a mechanical model for a thermal bimorph with many similarities to that derived here, but use the results of Doring *et al* to check their results, and do not include a thermal or dynamic model [13, 27]. Suh *et al* [10], Lin *et al* [8], and Wu and Hsu [11] all present mechanical models used to predict deflection but do not include thermal or dynamic models. Chan *et al* [2] presented a comprehensive mechanical and thermal model with some similarities to that presented here, but did not have experimental results to compare to their model predictions. Later work by the same group showed the ability to perform actuation with the structures but did not describe quantitative measurements of device performance [14]. Enikov and Lazarov [6] presented a comprehensive mechanical and thermal model of a similar device, but focused their experimental work on investigating time constants; they did not measure force or temperature. Chronis and Lee presented an SU-8 actuator with mechanical and thermal models and measured deflection, but did not measure force or frequency response [3]. Kim *et al* focused primarily on a force feedback system for cell manipulation and included measurements of gripping force and temperature, but did not include complete mechanical or thermal models [7].

The actuator described here differs in construction from most previous work by making use of the biocompatible polymer parylene C as a base material. The only other actuator of which we are aware that uses parylene C as a major structural component is the parylene gripper described by Zhou *et al* [14]. Zhou focused on applications of cell manipulation in an aqueous environment, and did not present data on measured force, temperature or displacement. The actuator described here extends such work by reporting the first set of characterization data for a micromachined parylene-based thermal actuator.

Although this paper focuses primarily on modeling and characterization, not applications, one particular application of interest for parylene devices is as microelectrode arrays for neural applications. Parylene is a preferred material for this application due to its long-term biocompatibility and barrier properties (e. g. [28, 29]). Parylene microelectrode arrays fabricated using a very similar process to that described here have recently been used for intramuscular electromyographic (EMG) recordings [30]. It may be useful to change the curvature of such electrode arrays during insertion to produce a better coupling to the muscles or nerves, similar to the methods described using shape memory allow structures [31]. The actuator presented here is a candidate for such a device.

In addition, in this paper we present mechanical, thermal and dynamic mathematical models side by side with the corresponding measurements. The models, validated in this fashion, can then be used with confidence for the design and optimization of thermal actuators for force, displacement, internal temperature and bandwidth. It is shown that the thermal time constant dominates the dynamics of the system. In addition, the linear model which is developed to describe the output force is shown to be sufficient for predicting actuator force over the operating range of the actuator.

2. Fabrication

The fabrication process for the microactuator is shown in figure 1. As a first step, 3.9 μm of parylene C is vapor deposited from the monomer at room temperature and a pressure of 35 mT (Specialty Coating Systems, PDS 2010 Labcoter®) on a ⟨1 0 0⟩ oriented silicon wafer. This layer of parylene C constitutes an optically transparent, flexible and insulating base for the devices, on top of which the metallic structures can be patterned. The primary metal

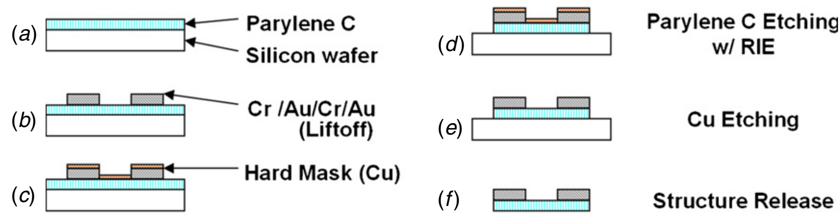

Figure 1. Fabrication process for microactuators (front cross-section view).

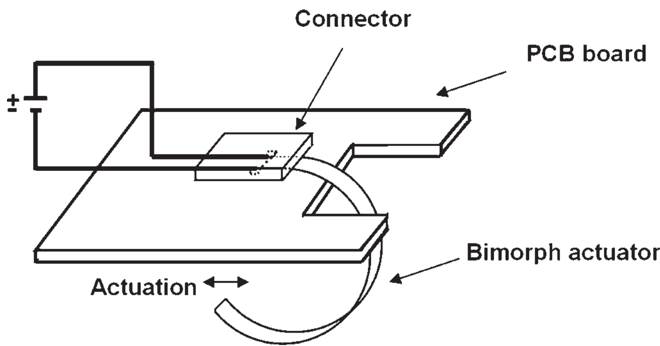

Figure 2. Schematic of the C-shaped microactuator design.

Table 2. Material properties used for modeling the device. Properties may vary from these values, particularly for the thin films [32–38].

Layer	1 (bottom)	2	3	4	5 (top)
Material	Parylene C	Cr	Au	Cr	Au
Thickness (μm)	3.9	0.03	0.5	0.5	0.03
Young's modulus (GPa)	2.76	140	80	140	80
CTE (ppm/°C)	35	6	14	6	14
Density (g cm^{-3})	1.29	7.19	19.3	7.19	19.3
Mass (ng)	189	8.09	361	135	21.7
Specific heat capacity (J g^{-1} C^{-1})	0.71	0.46	0.13	0.46	0.13

wires (500 nm Au and 500 nm Cr) within the device were created by dc sputtering and patterned with a lift-off process. However, bonding between parylene C and gold is poor, so a Cr adhesion layer (30 nm) was deposited before the gold deposition. Furthermore, Au (30 nm) was deposited to protect the Cr surface from oxidation and reduce contact resistance for the final device. This Au thin film drastically reduced the measured contact resistance of the device. For patterning of the parylene C layer, a sputtered Cu hard mask (100 nm) was patterned via liftoff, and the parylene was etched by reactive ion etching (RIE) using an O_2 plasma at 150 W and 300 mT. The Cu hard mask was then removed in a wet copper etchant. Finally, the device was manually peeled off from the silicon wafer. The adhesion between parylene and the silicon is strong enough to survive processing, but weak enough to allow the devices to peel off. Thus, no sacrificial layer or release process is needed, and stiction problems are avoided. This is a major advantage of the parylene process. After the structure's release, as shown in figure 2, the cantilever beam curls down into a 'C' shape due to different residual stresses in the various films.

3. Mechanical modeling

The thermal-operating cantilever microactuator consists of four metal layers and a parylene C layer, as shown in table 2 and figure 3. Three thick layers account for the majority of the mechanical structure: parylene (1), gold (3) and Cr (4). The bottom Cr is for adhesion, and the top Au gives a noble surface to wirebond to, reducing contact resistance. Mechanically, the actuator flattens up as the temperature of the device increases. The properties of table 2 will be used throughout the paper. The properties of parylene C were taken from the manufacturer's datasheet [32]. All the properties of the metals with the exception of elastic modulus were taken to be equal to the bulk properties from the ASM Metals Reference Book [33]. The elastic moduli of the metal thin films were taken from measurements on thin film devices [34, 35]. As is always the case with thin films, the material properties may vary from the bulk properties and depend on details of the deposition process. The reported values for the CTE and modulus of chromium and the elastic modulus of parylene C show significant variability in the literature (e.g. [36, 37]).

Timoshenko's bimetal thermostat theory [39] was extended to describe the behavior of the microactuator. This assumes that the structure is long compared to both width and the thickness. Each layer is indicated by the indexes 1, 2, 3, 4 and 5, respectively. The moments are taken about the bottom of the cross-section. In the static, zero load condition, the sum of the forces and moments are equal to zero. Furthermore, the longitudinal strain at the interface between each layer is equal. This can be expressed in the following equations. These equations can be solved simultaneously to compute the radius of curvature of the beam if the temperature is known, in the condition of zero external load. Due to residual stresses in the layers, the cantilever is curled into a 'C' shape at room temperature. The temperature at which the cantilever becomes flat is experimentally determined from the curvature at room temperature (20 °C). This temperature, T_{flat}, appears in the interface equation (3). For the device described in this paper, $T_{\text{flat}} = 60$ °C, by matching to the experimental data at 20 °C in figure 9

$$\sum_{n=1}^{5} P_n = 0 \tag{1}$$

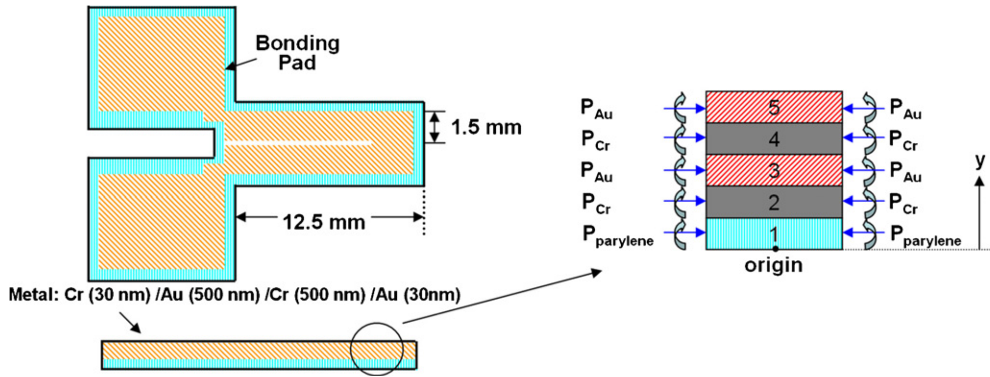

Figure 3. Illustration of a cantilever microactuator and its free-body diagram.

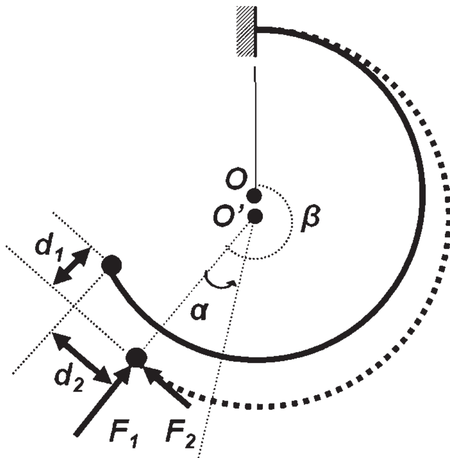

Figure 4. Diagram showing sign conventions and geometric quantities for the force calculation.

$$\sum M_o = \sum_{n=1}^{5} P_n y_n - \sum_{n=1}^{5} \frac{E_n I_n}{r} = 0 \qquad (2)$$

$$\alpha_n(T - T_{\text{flat}}) - \frac{P_n}{E_n t_n w} - \frac{t_n}{2r} = \alpha_{n-1}(T - T_{\text{flat}}) - \frac{P_{n-1}}{E_{n-1} t_{n-1} w} + \frac{t_{n-1}}{2r} \quad (n = 2 \ldots 5), \qquad (3)$$

where P_n is the axial load of each layer, which will change with temperature, E_n is the modulus of elasticity for each layer's material, $I_n = t_n{}^3 w/12$ is the area moment of inertia of each layer, r is the radius of curvature of the laminate beam which will change with temperature, t_n is the thickness of each layer, y_n is the position of the center of each layer with respect to the bottom of the beam, w is the width of the beam, T_{flat} is the temperature at which the cantilever becomes flat, T is the temperature of the cantilever and α_n is the thermal expansion coefficient of each layer's material.

For small displacements of the tip, the force can be computed by Castigliano's method [40]. Referring to figure 4,

$$d_i = \frac{\partial U}{\partial F_i}, \qquad (8)$$

where the deflection, d, that results from an applied force, F, can be computed by determining the rate of change of the strain energy with respect to the applied force in the same direction.

The stored strain energy for pure bending in a beam is

$$U = \int_0^L \frac{M^2}{2(EI)_{\text{eff}}} \mathrm{d}s, \qquad (9)$$

where M is the internal bending moment, L is beam length, $(EI)_{\text{eff}}$ is the effective bending rigidity of the composite beam, and $\mathrm{d}s = r\mathrm{d}\alpha$ is an increment along the length of the beam. This relationship is also valid for curved beams as long as the radius of curvature is large compared to the beam thickness, which is certainly true in this situation.

In order to compute the effective bending rigidity of the composite beam, first determine the position of the neutral axis [41]

$$y_c = \frac{\sum_{n=1} y_n E_n A_n}{\sum_{n=1} E_n A_n}, \qquad (4)$$

where $A_n = wt_n$ is the cross-section area of the nth layer.

The position of the center of the nth layer with respect to the neutral axis is therefore

$$z_n = y_n - y_c. \qquad (5)$$

The area moment of inertia about the neutral axis for the rectangular cross-section of each layer is then [40]

$$I_n = \frac{t_n^3 w}{12} + z_n^2 t_n w. \qquad (6)$$

Finally, the total effective flexural rigidity of the entire laminate is given by [42]

$$(EI)_{\text{eff}} = \sum_{n=1} E_n I_n. \qquad (7)$$

Now, applying Castigliano's theorem

$$d_i = \frac{\partial U}{\partial F_i} = \int_0^L \frac{M}{(EI)_{\text{eff}}} \frac{\partial M}{\partial F_i} \mathrm{d}s. \qquad (10)$$

Considering the static load balance, the internal moment is

$$M = F_1 r \sin\alpha + F_2 r(1 - \cos\alpha). \qquad (11)$$

The derivatives are easily evaluated:

$$\frac{\partial M}{\partial F_1} = r\sin\alpha, \qquad \frac{\partial M}{\partial F_2} = r(1 - \cos\alpha). \qquad (12)$$

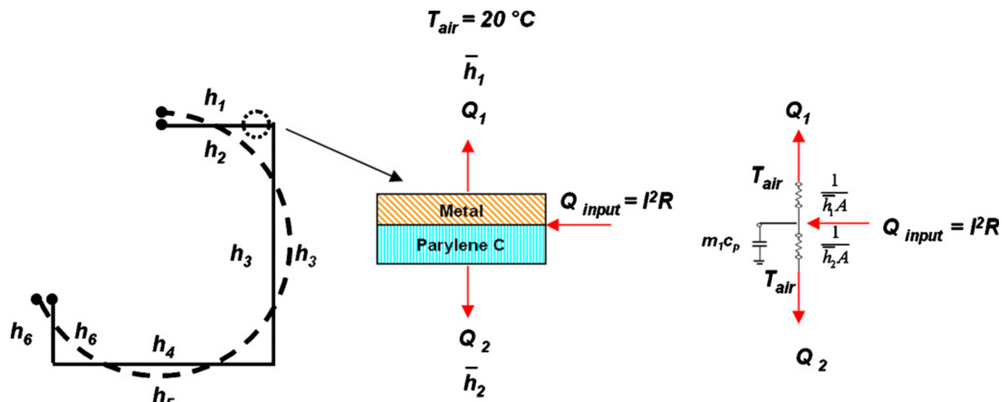

Figure 5. Schematic of the actuator and equivalent thermal circuit.

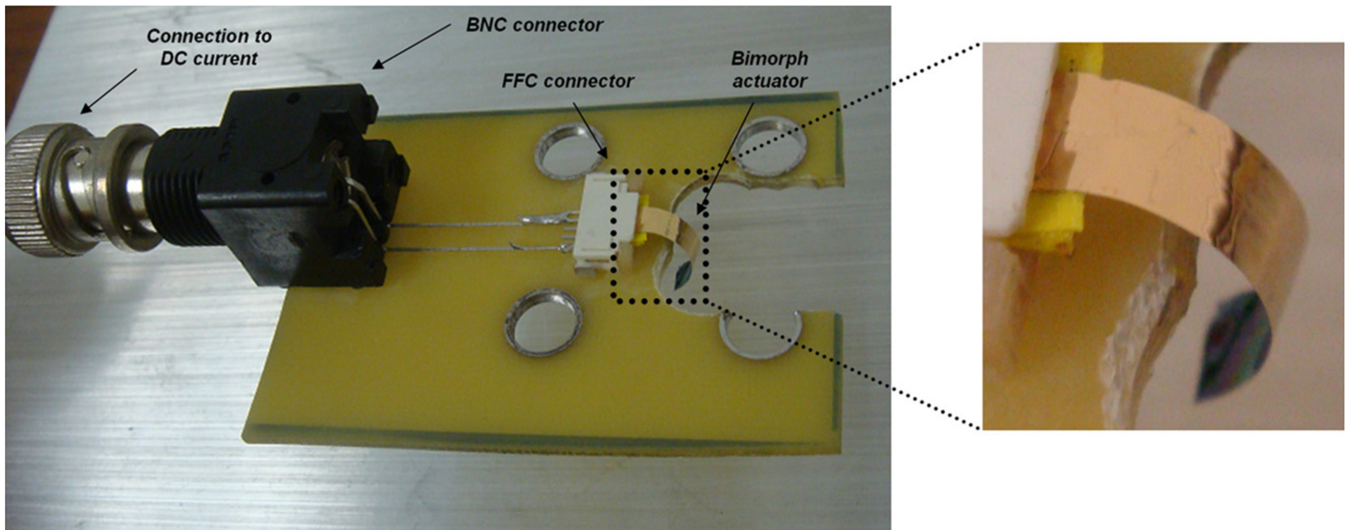

Figure 6. Actuator assembly and a close-up of the actuator.

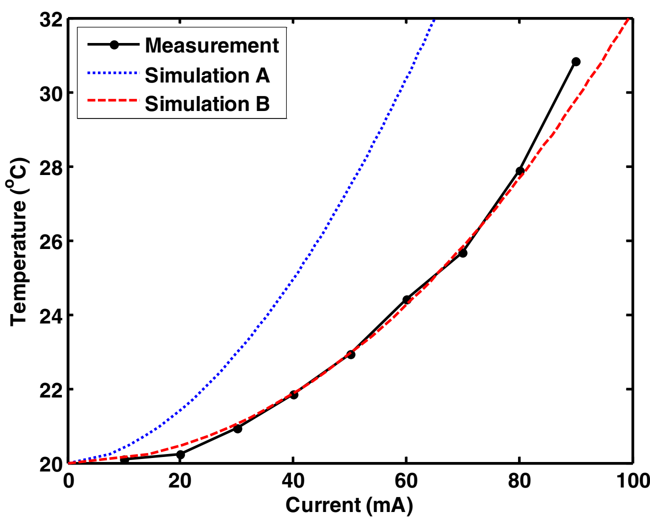

Figure 7. Internal device temperature at different dc current level during actuation (steady-state result). Simulation A uses the convection coefficient correlations in equations (18)–(20). Simulation B uses $\overline{h_1} = \overline{h_2} = 41$ W m^{-2} K^{-1}.

And the final result for displacements in response to the tip forces is

$$d_1 = \frac{r^3}{(EI)_{\mathrm{eff}}} \int_0^{\beta} [(F_1 \sin\alpha + F_2(1 - \cos\alpha)) \sin\alpha] \, \mathrm{d}\alpha,$$
$$d_2 = \frac{r^3}{(EI)_{\mathrm{eff}}} \int_0^{\beta} [(F_1 \sin\alpha + F_2(1 - \cos\alpha))(1 - \cos\alpha)] \, \mathrm{d}\alpha, \quad (13)$$

where d_i are the Cartesian deflections at the tip of the actuator. β is the angular extent of the curved actuator, and is equal to the total length divided by the radius of curvature ($\beta = L/r$). In order to maximize the range of validity of this linearized result, the value of β and r should be selected as an intermediate value between the value at the reference temperature and the value at the measurement temperature. For the results shown here, the arithmetic average is used, although it is not known if this is optimal. α is the angular coordinate used to express location along the circular beam.

By evaluating the integrals and solving for the forces, the following expressions are produced:

$$F_1 = \frac{(EI)_{\mathrm{eff}}[(6\beta + \sin(2\beta) - 4\sin(\beta))d_1 + (8\sin^2(\beta/2) - 2\sin^2(\beta))d_2]}{r^3(\beta\sin(2\beta) - 3\beta^2 - 7\sin^2(\beta) + 4\beta\sin(\beta) + 16\sin^2(\beta/2))}$$
$$F_2 = \frac{(EI)_{\mathrm{eff}}[(8\sin^2(\beta/2) - 2\sin^2(\beta))d_1 + (\sin(2\beta) - 2\beta)d_2]}{r^3(\beta\sin(2\beta) - 3\beta^2 - 7\sin^2(\beta) + 4\beta\sin(\beta) + 16\sin^2(\beta/2))}. \quad (14)$$

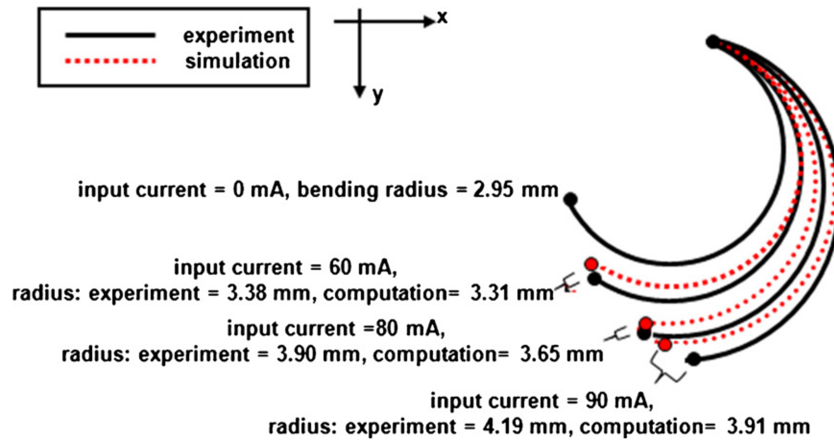

Figure 8. Shape profile of the actuator at each current level during actuation.

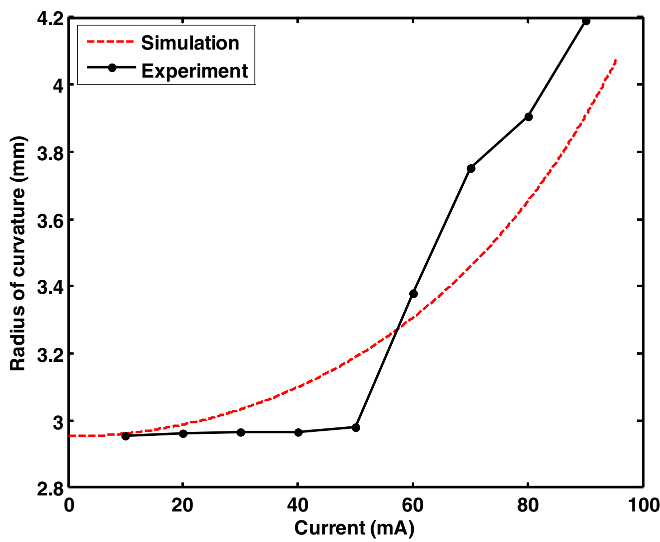

Figure 9. Measurements of the radius of the curvature of the actuator compared to simulation.

Using (14), it is now possible to compute the force for a known deflection. In the experimental case discussed below, the tip of the cantilever is held fixed as temperature varies. Since temperature causes the radius of curvature to vary, which would create motion of the tip, deflection, d, must be nonzero in order to keep the actuator tip at the fixed position. The required deflection to accomplish this is computed by comparing the tip position for the free cantilever with radius of curvature r, to the tip position for the undeflected cantilever with radius of curvature r_0:

$$\begin{aligned} d_1 &= r - [r_0 \cos(\beta_0 - \beta) - (r - r_0)\cos(\beta - \pi)] \\ d_2 &= (r - r_0)\sin(\beta - \pi) + r_0 \sin(\beta_0 - \beta). \end{aligned} \tag{15}$$

Computation of the blocked force proceeds by first determining the final and initial radii of curvature from equations (1) through (3) using the final and initial temperatures, respectively. These radii of curvature are used in equation (15), recognizing that $\beta = L/r$ and $\beta_0 = L/r_0$, to compute the tip deflections that would result if the tip were free to move, d_1 and d_2. Finally, in the blocked case, the forces required to bring the tip back to its initial position can be computed from equation (14), using the average r and β. It is important to note that the force computation relies on Castigliano's theorem, which is only valid for small deflections. Hence, it is expected that as temperature increases, the measured force may deviate from the force predicted by these relationships.

4. Thermal-electrical modeling

For thermal modeling, an analogy is made between thermal systems and electrical systems, as shown in figure 5. The metal layers generate heat due to Joule heating, represented by Q_{in}. The heat flows through the thickness and is lost to the environment through convection. Convection on the metal and parylene surfaces is modeled using an average thermal resistance, $1/(\bar{h}_1 A)$ and $1/(\bar{h}_2 A)$, respectively. Since the device is very thin compared to its length and width, the assumption is made that heat flow through the thickness is large in relation to that in the other directions.

The identical cross-section and large aspect ratio of these devices allows the material to be considered uniform temperature in the plane of the devices. Analysis of the Biot number also indicates that the temperature of the structure is uniform through the thickness at any instant of time when the following condition is met:

$$Bi = \frac{\bar{h}L}{k} < 0.1, \tag{16}$$

where making a conservative estimate, $L = 2.5\ \mu$m is half the thickness of the structure, $k > 0.084$ W m^{-1} K^{-1} is the thermal conductivity of the parylene, $\bar{h} < 100$ W m^{-2} K^{-1} is the average convection heat transfer coefficient, and Bi is the Biot number. For the devices described here, then, $Bi < 0.003$, justifying the uniform temperature model. In order to model the dynamics as a function of input current, a transient heat transfer equation is used, based on the equivalent thermal circuit (figure 5):

$$\sum_n m_n (c_p)_n \frac{\mathrm{d}T}{\mathrm{d}t} + \frac{T - T_{\text{air}}}{\frac{1}{\bar{h}_1 A_1}} + \frac{T - T_{\text{air}}}{\frac{1}{\bar{h}_2 A_1}} = I^2 R, \tag{17}$$

where m_n is the mass of the nth layer, $(c_p)_n$ is the specific heat capacity of the nth layer, $\mathrm{d}T/\mathrm{d}t$ is the temperature time rate of change, $\overline{h_1}$ is the area averaged convection heat transfer coefficient at the metal surfaces, $\overline{h_2}$ is the area averaged

convection heat transfer coefficient at the parylene surfaces, A is the surface area of one side of the actuator, I is the input current, T_{air} is environmental temperature = 20 °C and R is the total electrical resistance of the actuator.

To obtain an estimate for the average convection heat transfer coefficient, the curved structure was initially approximated as four flat segments, as shown in figure 5. The correlations for natural convection from flat plates from Incropera *et al* and Chambers *et al* were used to estimate the convection heat transfer coefficient on each surface [43–45]. For the horizontal plates, the Rayleigh number is computed based on the half plate width of $w/2 = 1.5$ mm since this is what Chambers uses. For the vertical plate, the Rayleigh number is based on the vertical length of the plate, as described by Incropera *et al*. Chambers suggests that equations (18) and (19) are valid for $86 < Ra < 1400$, and his calculations are two dimensional. In our experiments, Ra ranges from approximately 1–100, and the heat transfer is three dimensional. Thus, there is concern that the correlations may underestimate the heat transfer coefficients. This is borne out by experimental results later in the paper, in agreement with the findings of some other authors working on microscale heat transfer:

$$\overline{\mathrm{Nu}}_{w/2} = 0.653(Ra_{w/2})^{0.143} \text{ (upper surface of heated plate)} \tag{18}$$

$$\overline{\mathrm{Nu}}_{w/2} = 0.979(Ra_{w/2})^{0.137} \text{ (lower surface of heated plate)} \tag{19}$$

$$\overline{\mathrm{Nu}}_{L} = \left(0.825 + \frac{0.387 Ra_L^{1/6}}{[1 + (0.492\,\mathrm{Pr})^{9/16}]^{8/27}}\right)^2 \text{ (sidewall)}, \tag{20}$$

where Ra is the Rayleigh number, Pr is the Prandtl number, and Nu is the Nusselt number. Ra, Nu and h vary as a function of temperature [45].

For the device described here, at an actuator temperature of $T = 26$ °C, which is the average operating temperature in our experiments, and an ambient temperature of 20 °C, values are obtained for $\overline{\mathrm{Ra}}$ and $\overline{\mathrm{Nu}}$, resulting in the convection coefficients shown in table 3. Varying the surface temperature from 23 to 35 °C results in variations of the convective heat transfer parameters on the order of ±10%. As the actuator deforms, it is also possible that the convection coefficients will change, since natural convection is dependent on the orientation with respect to gravity. Absolute maximum changes are expected to be on the order of 25%, based on the difference between lower (h_2 and h_5) and upper or vertical (h_1, h_3, h_4, h_6) convection coefficients. This is not expected to be a strong effect.

The surface of the actuator is highly reflective due to the sputtered metal films. Radiation from the surface at a temperature of 26 °C to an ambient at 20 °C, as computed for a black body with a surface emissivity of 0.1, contributes only an additional 3% to 4% to the effective convective heat transfer coefficient, and so will be neglected. The resulting total heat transfer coefficient is attained by area averaging the results in table 3, giving $\overline{h_1} = \overline{h_2} = 15.9$ W m^{-2} K^{-1}, with total surface area on each side of the actuator, $A = wL = 37.5$ mm^2.

Table 3. Predicted area averaged convection heat transfer coefficient, as computed using correlations, and surface area of each portion of the actuator as shown in figure 5.

	1	2	3	4	5	6
$\bar{h}$(W m^{-2} K^{-1})	12.5	18.7	12.8	12.5	18.7	19.6
A (μm^2)	6.3	6.3	12.6	12.6	12.6	6.3

5. Experimental result

Figure 6 shows a photograph of the set-up of the experiment and a close-up of a microactuator, respectively. The actuation system in the middle of the photograph consists of a PCB, a BNC connector, an FFC connector and a C-shape actuator. It is observed that at room temperature (20 °C), the end of the actuator bends down from the connector, due to in-built residual stresses. We characterized temperature, shape change, force and the frequency response of force during actuation.

First, consider the results of experiments on temperature change while driving a dc current (10–90 mA). Device temperature was investigated, based on the dc resistance of the device at each current, which is an indication of the internal temperature of the device. In order to correlate resistance to temperature, the resistance of the actuator was first measured in an iso-temperature oven at a series of temperatures. Oven temperature was determined by a thermocouple placed in the oven near the device. The resistance of the wires without the actuator in place was also measured and subtracted out from the total resistance. The actuator was then removed from the oven, and driven by a dc current over 10–90 mA range. The resistance of the actuator varied quadratically with drive current from 3.585 to 3.713 Ω, correlating to an internal temperature of 20.2–30.8 °C, as shown in figure 7.

In addition to experimental data on temperature versus current, two simulations are shown in figure 7, using the thermal model in figure 5 and equation (17). In simulation A, the convection heat transfer coefficient h varies as a function of temperature, as described above using the correlations in (18)–(20). Simulation B uses a fixed average convective heat transfer coefficient of $\overline{h_1} = \overline{h_2} = 41$ W m^{-2} K^{-1} to achieve the best fit to experiment. In both simulations, the resistance varies linearly with temperature from 3.585 to 3.713 Ω over the 20.2–30.8 °C range. Because of the relationship between current and Joule heating, the current-temperature characteristic is parabolic. It is seen that the one-dimensional, convection dominated model captures the main thermal features of the response. However, as noted by other authors (e.g. [46, 47]) the natural convection coefficient experienced by the MEMS device in this low Rayleigh number regime is larger than would be expected based on macroscale correlations. This is in agreement with the results of Hu *et al*, who demonstrated that conduction is of greater importance at the microscale and suggest an effective convective heat transfer coefficient of 35 W m^{-2} K^{-1}, similar to that obtained here [47].

Figure 8 shows the shape change of the actuator during operation while driving a dc current from 10–90 mA with no external mechanical load. When the actuator was heated by the driving current, it flattened up. Each steady state

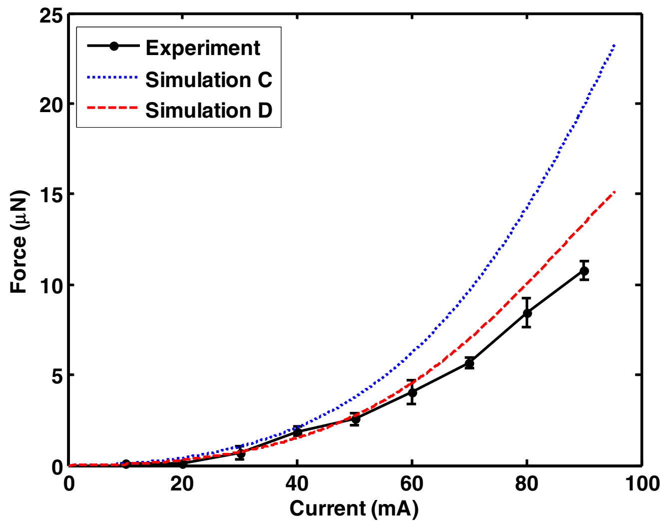

Figure 10. Lifting force (F_1) measurement of the actuator compared to simulation. Simulation C assumes no lateral slipping and uses equations (14) and (15). Simulation D assumes no lateral force, and uses equations (21) and (15).

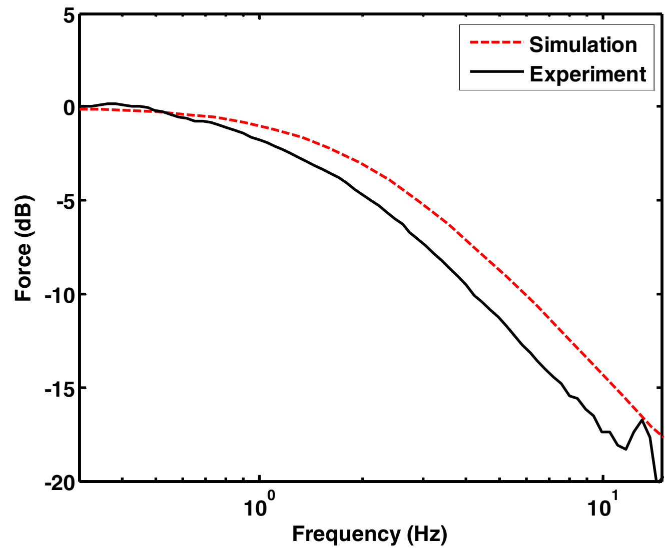

Figure 11. Measured frequency response of lifting force (F_1) during actuation compared to a first-order model dominated by thermal effects.

shape change was photographed by a camera. Using image processing (pixel size: 41 μm), the radius of curvature of the actuator was calculated at each temperature, using the positions of three points on the actuator. The radius of curvature of the actuator varied quadratically from 2.95 mm to 4.19 mm as the driving current increased. The maximum displacement of the tip was 3.18 mm along the x-direction and 4.22 mm along the y-direction (at $I = 90$ mA). Figure 9 shows the radius of the curvature of the actuator at each current level during actuation. Simulation data on the radius of curvature of the cantilever beam is also reported, using the thermal model B with $\overline{h_1} = \overline{h_2} = 41$ W m^{-2} K^{-1} to compute steady state temperature, followed by application of the mechanical model of equations (1)–(3) to compute the radius of curvature. The theoretical displacement response agrees well with the experimental result, indicating that the zero load mechanical model captures the primary features of the static mechanics.

Finally, static tip lifting force (F_1) measurements of the actuator were collected while driving a dc current (10–90 mA). The actuation force was measured with a Femto Tools® force sensor (Model: FT-S540). This is a MEMS-based uniaxial force sensor with a dynamic range of 180 μN, a resolution of less than 1 μN, and a tip size of 50 μm × 50 μm. The axial spring constant for the sensor is approximately 150 N m^{-1}, considerably stiffer than the C-shaped actuator, which has a stiffness of 0.57 N m^{-1}. Thus, this experiment is a blocked situation where the perpendicular motion of the C-shape actuator tip is constrained to be essentially zero. The lateral motion of the tip is more difficult to determine. If the actuator does not slip laterally with respect to the force sensor, and the force sensor lateral compliance is high enough, then the lateral displacement of the tip will also be zero, which is the assumption used previously to compute the force as described by equations (14) and (15). The results of applying this model are shown in figure 10 as simulation C. However, the coefficient of static friction between the force sensor tip and the actuator is not known, and it is possible that they slip relative to each other. In addition, the force sensor has substantially more lateral compliance than axial compliance, and may partially deflect in response to the lateral force, resulting in lateral tip motion. In the limit, the lateral force on the actuator, F_2 in figure 4, will be zero. In such a condition, equation (14) simplifies to

$$F_1 = \frac{(EI)_{\text{eff}}}{r^3\,(\beta/2 + (1/4)\sin(2\beta))} d_1. \tag{21}$$

The result using equation (21) is shown in figure 10 as simulation D.

The tip of the force sensor was first slightly contacted to the body of the actuator, until an increase of sensor output was observed (<1 μN). Then, the actuator was heated with a driving dc current. The experimental set-up was covered by a box to minimize the effect of air movement in the room. Over the 10–90 mA range, the force of the actuator changed from less than 1–10.7 μN, as shown in figure 10.

In order to determine the bandwidth of the actuator, the frequency response of the tip force was investigated using the Femto Tools® force sensor. The frequency response was measured by driving a sinusoidal voltage at 0.25 peak (70 mA peak current). The drive frequency varied from 0.1–20 Hz. Since force is proportional to the square of the current, the force response is at twice the drive frequency. Using Fourier techniques, the magnitude of the force was measured at twice the drive frequency.

Referring back to the thermal model of equation (17), if thermal dynamics dominate, then the system is expected to have a first-order low-pass frequency response for force

relative to current squared with a bandwidth determined by the thermal time constant

$$\tau = \frac{\sum_n [m_n (c_p)_n]}{(\bar{h}_1 + \bar{h}_2) A}, \quad (22)$$

where the bandwidth in hertz will be $f = 1/(2\pi\tau)$. Figure 11 shows the measured frequency response compared to a first-order model with the computed bandwidth. The model predicts a bandwidth of 1.96 Hz, using thermal model B with $\overline{h_1} = \overline{h_2} = 41$ W m^{-2} K^{-1}. The measured 3 dB bandwidth is 1.41 Hz. The good agreement between the modeled and measured bandwidth suggests that the dynamics are dominated by the thermal time constant.

These results suggest that in order to increase the actuation bandwidth, the thermal time constant must be reduced. This can be accomplished by reducing the thickness of some of the layers. For example, reducing the parylene thickness to 1 μm is expected to result in an increase in bandwidth to 3.3 Hz. Of course, such changes will also modify the static shape, force characteristics and deflection characteristics of the actuator according to the models developed above.

6. Conclusion

A C-shape bimorph actuator which consists of parylene C and multiple metal layers has been developed, modeled and characterized. This actuator flattens up due to differential thermal expansion of the materials when it is powered by a driving current. This device operates at less than 0.33 V input voltage and 90 mA input current. During operation, the temperature of the actuator is less than 32 °C. This actuator has 11 μN load capacity and its bandwidth is 1.4 Hz.

Three performance metrics were introduced (displacement, operation temperature and force) that characterize the actuator. Mathematical modeling for these performance metrics was carried out, using beam theory and a heat transfer model. The simulation results agree well with the experimental results, showing that the dynamics of the system are dominated by the convection driven heat transfer and that a circular bending beam model is sufficient for predicting the actuator force and deflection. As reported by other authors, we find that the effective convection coefficient for this low Rayleigh number device is higher than would be predicted by correlations developed for higher Rayleigh number regimes.

Acknowledgments

Authors would like to thank all the members of the Tufts Micro and Nanofabrication Facility for their help. This work was supported by DARPA under contract W911SR-08-C-0012.

References

[1] Ataka M, Omodaka A, Takeshima N and Fujita H 1993 Fabrication and operation of polyimide bimorph actuators for a ciliary motion system *J. Microelectromech. Syst.* **2** 146–50

[2] Chan H Y and Li W J 2003 A thermally actuated polymer micro robotic gripper for manipulation of biological cells *IEEE Int. Conf. on Robotics and Automation, ICRA '03* pp 288–93

[3] Chronis N and Lee L P 2005 Electrothermally activated SU-8 microgripper for single cell manipulation in solution *J. Microelectromech. Syst.* **14** 857–63

[4] Comtois J H and Bright V M 1997 Applications for surface-micromachined polysilicon thermal actuators and arrays *Sensors Actuators* A **58** 19–25

[5] Ebefors T, Mattsson J U, Kalvesten E and Stemme G 2000 A robust micro conveyer realized by arrayed polyimide joint actuators *J. Micromech. Microeng.* **10** 337–49

[6] Enikov E T and Lazarov K 2003 PCB-integrated metallic thermal micro-actuators *Sensors Actuators* A **105** 76–82

[7] Kim K, Liu X, Zhang Y and Sun Y 2008 Nanonewton force-controlled manipulation of biological cells using a monolithic MEMS microgripper with two-axis force feedback *J. Micromech. Microeng.* **18** 055013

[8] Lin G, Kim C J, Konishi S and Fujita H 1995 Design, fabrication, and testing of a C-shape actuator *8th Int. Conf. on Solid State Sensors and Actuators and Eurosensors IX* pp 416–9

[9] Riethmuller W and Benecke W 1988 Thermally excited silicon microactuators *IEEE Trans. Electron Devices* **35** 758–63

[10] Suh J W, Glander S F, Darling R B, Storment C W and Kovacs G T A 1997 Organic thermal and electrostatic ciliary microactuator array for object manipulation *Sensors Actuators* A **58** 51–60

[11] Wu C T and Hsu W 2006 Design and fabrication of an electrothermal microactuator for multi-level conveying *Microsyst. Technol.* **12** 293–8

[12] Kladitis P E and Bright V M 2000 Prototype microrobots for micro-positioning and micro-unmanned vehicles *Sensors Actuators* A **80** 132–7

[13] Doring C, Grauer T, Marek J, Mettner M S, Trah H P and Willmann M 1992 Micromachined thermoelectrically driven cantilever structures for fluid jet deflection *Microelectromechanical Systems, MEMS '92* pp 12–8

[14] Zhou J W L, Chan H Y, To T K H, Lai K W C and Li W J 2004 Polymer MEMS actuators for underwater micromanipulation *IEEE/ASME Trans. Mechatronics* **9** 334–42

[15] Hirata T, Akashi T, Bertholds A, Gruber H P, Schmid A, Gretillat M A, Guenat O T and De Rooij N F 1998 A novel pneumatic actuator system realised by microelectro-discharge machining *11th Annu. Int. Workshop on Micro Electro Mechanical Systems, MEMS '98* pp 160–5

[16] Jeong O C and Konishi S 2006 All PDMS pneumatic microfinger with bidirectional motion and its application *J. Microelectromech. Syst.* **15** 896–903

[17] Konishi S and Fujita H 1994 A conveyance system using air flow based on the concept of distributed micro motion systems *J. Microelectromech. Syst.* **3** 54–8

[18] Pister K S J, Fearing R S and Howe R T 1990 A planar air levitated electrostatic actuator system *IEEE Micro Electro Mechanical Systems, MEMS '90* pp 67–71

[19] DeVoe D L and Pisano A P 1997 Modeling and optimal design of piezoelectric cantilever microactuators *J. Microelectromech. Syst.* **6** 266–70

[20] Meng Q, Mehregany M and Deng K 1993 Modeling of the electromechanical performance of piezoelectric laminated microactuators *J. Micromech. Microeng.* **3** 18

[21] Akiyama T, Collard D and Fujita H 1997 Scratch drive actuator with mechanical links for self-assembly of three-dimensional MEMS *J. Microelectromech. Syst.* **6** 10–7

[22] Tang W C, Nguyen T C H, Judy M W and Howe R T 1990 Electrostatic-comb drive of lateral polysilicon resonators *Sensors Actuators* A **21** 328–31

[23] Nakazawa H, Watanabe Y, Morita O, Edo M and Yonezawa E 1997 The two-dimensional micro conveyer: principles and fabrication process of the actuator *Solid State Sensors and Actuators, TRANSDUCERS '97* pp 33–6

[24] Chang L, Tsao T, Yu-Chong T, Wenheng L, Will P and Chih-Ming H 1995 A micromachined permalloy magnetic actuator array for micro robotics assembly systems *Solid-State Sensors and Actuators and Eurosensors IX, Transducers '95* pp 328–31

[25] Gill J J, Chang D T, Momoda L A and Carman G P 2001 Manufacturing issues of thin film NiTi microwrapper *Sensors Actuators* A **93** 148–56

[26] Kim B, Lee M G, Lee Y P, Kim Y and Lee G 2006 An earthworm-like micro robot using shape memory alloy actuator *Sensors Actuators* A **125** 429–37

[27] Chu W H, Mehregany M and Mullen R L 1993 Analysis of tip deflection and force of a bimetallic cantilever microactuator *J. Micromech. Microeng.* **3** 4–7

[28] Loeb G E, Bak M J, Salcman M and Schmidt E M 1977 Parylene as a chronically stable, reproducible microelectrode insulator *IEEE Trans. Biomed. Eng.* **24** 121–8

[29] Schmidt E M, McIntosh J S and Bak M J 1988 Long-term implants of Parylene-C coated microelectrodes *Med. Biol. Eng. Comput.* **26** 96–101

[30] Metallo C, White R D and Trimmer B A 2011 Flexible parylene-based microelectrode arrays for high resolution EMG recordings in freely moving small animals *J. Neurosci. Methods* **195** 176–84

[31] Takeuchi S and Shimoyama I 2000 A three-dimensional shape memory alloy microelectrode with clipping structure for insect neural recording *J. Microelectromech. Syst.* **9** 24–31

[32] Frados J 1968 *Modern Plastics Encyclopedia* (New York: McGraw-Hill)

[33] Bauccio M 1993 *ASM Metals Reference Book* 3rd edn (Materials Park: ASM International)

[34] Halg B 1990 On a nonvolatile memory cell based on micro-electro-mechanics *IEEE Micro Electro Mechanical Systems, MEMS '90* pp 172–6

[35] Rashidian B and Allen M G 1993 Electrothermal microactuators based on dielectric loss heating *IEEE Micro Electro Mechanical Systems, MEMS '93* pp 24–9

[36] Harder T A, Yao T J, He Q, Shih C Y and Tai Y C 2002 Residual stress in thin-film Parylene-C *IEEE Micro Electro Mechanical Systems, MEMS '02* pp 435–8

[37] Janda M 1986 On the intrinsic stress in thin chromium films *Thin Solid Films* **142** 37–45

[38] Shackelford J F and Alexander W 2001 *CRC Materials Science and Engineering Handbook* (Boca Raton, FL: CRC Press)

[39] Timoshenko S 1925 Analysis of bi-metal thermostats *J. Opt. Soc. Am. Rev. Sci. Instrum.* **11** 233–55

[40] Budynas R G 1999 *Advanced Strength and Applied Stress Analysis* 2nd edn (Boston, MA: WCB/McGraw-Hill)

[41] Pilkey W D 1994 *Formulas for Stress, Strain, and Structural Matrices* (New York: Wiley)

[42] Crandall S H, Dahl N C and Lardner T J 1978 *An Introduction to the Mechanics of Solids* 2nd edn (New York: McGraw-Hill)

[43] Chambers B and Tien-Yu T L 1997 A numerical study of local and average natural convection Nusselt numbers for simultaneous convection above and below a uniformly heated horizontal thin plate *J. Heat Transfer* **119** 102–8

[44] Churchill S W and Chu H H S 1975 Correlating equations for laminar and turbulent free convection from a horizontal cylinder *Int. J. Heat Mass Transfer* **18** 1049–53

[45] Incropera F P and DeWitt D P 1996 *Fundamentals of Heat and Mass Transfer* 4th edn (New York: Wiley)

[46] Guo Z-Y and Li Z-X 2003 Size effect on microscale single-phase flow and heat transfer *Int. J. Heat Mass Transfer* **46** 149–59

[47] Hu X J, Jain A and Goodson K E 2008 Investigation of the natural convection boundary condition in microfabricated structures *Int. J. Therm. Sci.* **47** 820–4